

1 **Revision 1:**

2 (final accepted version)

3 **Magnetite–apatite deposit from Sri Lanka:**  
4 **implications on Kiruna-type mineralization**  
5 **associated with ultramafic intrusion and mantle**  
6 **metasomatism**

7 **Xiao-Fang He<sup>1,2</sup>, M. Santosh<sup>1,2,3\*</sup>, T. Tsunogae<sup>4,5</sup>, Sanjeeva P.K. Malaviarachchi<sup>6</sup>**

8 <sup>1</sup> *School of Earth Sciences and Resources, China University of Geosciences Beijing, No. 29 Xueyuan Road,*  
9 *Haidian District, Beijing, 100083, China*

10 <sup>2</sup> *Department of Earth Sciences, School of Physical Sciences, University of Adelaide, Adelaide, SA 5005,*  
11 *Australia*

12 <sup>3</sup> *State Key Laboratory of Continental Dynamics, Department of Geology, Northwest University, Xi'an 710069,*  
13 *China*

14 <sup>4</sup> *Faculty of Life and Environmental Sciences, University of Tsukuba, Ibaraki 305-8572, Japan*

15 <sup>5</sup> *Department of Geology, University of Johannesburg, Auckland Park 2006, South Africa*

16 <sup>6</sup> *Department of Geology, Faculty of Science, University of Peradeniya, Peradeniya 20400, Sri Lanka*

17 *\*Corresponding author e-mail: [msantosh.gr@gmail.com](mailto:msantosh.gr@gmail.com)*  
18

19 **ABSTRACT**

20 Kiruna-type iron oxide–apatite associations occur in a variety of rock types and their  
21 origin has remained controversial. Most of the Kiruna-type deposits are associated with  
22 intermediate to felsic rocks, and in rare cases with ultramafic rocks. Here we investigate the  
23 Seruwila iron oxide–apatite deposit at the contact between the Highland and Vijayan  
24 complexes which has been defined as the ‘eastern suture’ in Sri Lanka which formed during  
25 the late Neoproterozoic assembly of the Gondwana supercontinent. The ore deposit is hosted  
26 in an ultramafic intrusion and comprises massive and disseminated mineralization. The ore-  
27 bearing rocks are mainly composed of low-Ti magnetite and chlor-fluorapatite. Our

28 petrological and geochemical studies suggest a magmatic–hydrothermal model for the  
29 mineralization wherein: 1) the Cl-rich magmatic–hydrothermal fluid scavenged iron and P  
30 from the ultramafic magma, transported iron to shallower levels in the crust and deposited  
31 along the suture zone to form the massive type magnetite and apatite; and 2) the cooling of  
32 the hydrothermal fluids resulted in the growth of disseminated magnetite and the precipitation  
33 of sulfide minerals, followed by a calcic metasomatism (scapolitization and actinolitization).  
34 This model is in conformity with the genetic relation between Kiruna-type deposits and iron  
35 oxide–copper–gold (IOCG) deposits. We also report LA–ICP–MS zircon U–Pb ages from the  
36 host ultramafic intrusion suggesting its emplacement at ca. 530 Ma, which is younger than  
37 the regional high-grade metamorphism associated with the collisional assembly of the crustal  
38 blocks in Sri Lanka at ca. 540 Ma. By analogy with the common occurrence of Kiruna-type  
39 deposits in extensional tectonic settings, and the geochemical features of the studied rocks  
40 including low silica, high Mg, Fe, Ca with high field strength elements (HFSEs) (Nb, Ta, Zr,  
41 Hf, Ti) depletion and strong LREE, F enrichment, we envisage that the ultramafic  
42 magmatism occurred in a post-collisional extensional setting derived from a volatile- and  
43 LREE-rich metasomatized lithospheric mantle.

44 **Key words:** Kiruna-type; IOA deposits; magnetite; apatite; ultramafic intrusion; Sri Lanka

## 45 INTRODUCTION

46 Kiruna-type iron oxide–apatite (IOA) deposits are important sources of Fe and P, and  
47 occur in a variety of geological settings such as those in Sweden, Iran, American Cordillera,  
48 and China (Herz and Valentine 1970; Hou et al. 2012; Jonsson et al. 2013; Sabet-Mobarhan-  
49 Talab et al. 2015). They share common mineralogical features dominated by low-Ti  
50 magnetite with variable amounts of apatite but poor in quartz (Tornos et al. 2016). They also  
51 generally display a close relationship with alkali-calcic intermediate to felsic rocks. The

52 origin of IOA deposit is still debated. Some workers favor a magmatic model due to the close  
53 genetic relationship of the Kiruna-type magnetite–apatite mineralization with igneous suites  
54 (Park 1961; Henriquez and Martin 1978; Naslund et al. 1998), whereas others favor a  
55 hydrothermal origin based on evidence from fluid inclusions, replacement texture and  
56 metasomatic zones (Barton and Johnson 1996; Murray and Oreskes 1997; Simon et al. 2004;  
57 Dare and Beaudoin 2015). Recent studies have proposed an integrated magmatic–  
58 hydrothermal model (e.g. Taghipour et al. 2015; Knipping et al. 2015; Tornos et al. 2016),  
59 which also confirms the genetic connection between Kiruna-type IOA and iron oxide–  
60 copper–gold (IOCG) deposits, in which IOA deposits represent the deeper roots of the IOCG  
61 systems (e.g. Sillitoe, 2003).

62 Occurrence of Kiruna-type iron oxide–apatite (IOA) rocks in ultramafic rocks are rare.  
63 Only a few examples have been reported including fluoro-hydroxyl-apatite associated with  
64 chlorite-talc schists located in the margin of small ultramafic bodies in Georgia and Maryland,  
65 USA (Herz and Valentine 1970), and small concentrations of magnetite–apatite rocks in  
66 ophiolite complexes (Orthys Complex, Greece; Mitsis and Economou-Eliopoulos 2001;  
67 Lizard Complex, UK; Hopkinson and Roberts 1999). However, most of these are small-scale  
68 deposits.

69 The Seruwila magnetite–apatite deposit occurs along the tectonic contact between the  
70 Vijayan and Highland Complexes which is interpreted as a mineralized domain along a  
71 Neoproterozoic suture zone, also referred to as the “eastern suture” in Sri Lanka, (e.g. He et  
72 al. 2016). The ore-bearing rocks are mainly composed of magnetite and apatite in various  
73 proportions, hosted in an ultramafic intrusion with cumulate features. Although this deposit  
74 has no world-class economic value given its relatively small size as compared to other iron  
75 deposits, it stands as the unique example of a Kiruna-type IOA deposit associated with  
76 ultramafics within a Gondwana-aged suture. In addition, the Seruwila IOA deposit is



101 Highland Complex (HC) is dominantly composed of Archean–Paleoproterozoic  
102 metasedimentary rocks, with interbedded quartzites and pelites in the metasedimentary belt,  
103 which were intruded by both felsic and mafic sills and dykes (Kröner and Jaeckel, 1994;  
104 Braun and Kriegsman, 2003; Santosh et al. 2014; Takamura et al. 2015). Rocks of both VC–  
105 HC series underwent high-grade metamorphism during Late Neoproterozoic to early  
106 Cambrian (Dharmapriya et al. 2015; He et al. 2016 and references therein).

107 The Vijayan–Highland Complex (VC–HC) preserves evidence for typical rock  
108 association developed in subduction-related settings including metachert, serpentinitised  
109 ultramafic units, and metabasalts (He et al. 2016). Cr–Ni serpentinites (Fig.1) near Ussangoda  
110 (Rajapaksha et al. 2012; He et al. 2016), Cu-sulphide deposits (Dissanayake and  
111 Weerasooriya 1986), massive magnetite–hematite deposit at Wellawaya, also occur along the  
112 boundary between the VC and HC in addition to the IOA-type deposit at Seruwila  
113 (Jayawardena, 1982). The abundance of mineralization support the notion that the suture is a  
114 persistently mineralized domain.

### 115 **The Seruwila iron oxide–apatite deposit ore geology**

116 The study area of Seruwila is located in the Trincomalee District about 275 kilometers  
117 from Colombo (Fig. 1). The dominant basement rocks in this area are charnockites  
118 (orthopyroxene-bearing anhydrous granulites) and quartzite (HC) and metagranites and  
119 amphibole–biotite gneisses to the southeast (VC). The mineralization at Seruwila occurs at  
120 the eastern boundary between the HC and the VC (Fig. 2a).

121 The massive or scattered ores in Seruwila occur as well-defined lenticular pods within  
122 ultramafic rocks. They are cut across by a group of normal faults (Fig. 2b). The magnetite-  
123 bearing ultramafic rocks occur as discontinuous and disrupted layers with length ranging  
124 from 1 to 5 meters, and the weathered surfaces contain secondary copper minerals such as  
125 malachite and azurite (Fig. 2b). Coarse scapolite crystals range up to 2 cm in length in the

126 ultramafic intrusion–ore deposit transition zone. Clinopyroxene-bearing intermediate rocks  
127 (enderbite) constitute the major basement rock in the deposit area showing a sharp contact  
128 with the ultramafic rocks and contains no ore mineral (Jayawardena, 1982). The  
129 clinopyroxene-bearing rocks show alkaline features and has an emplacement age of  $924 \pm 10$   
130 Ma with metamorphism at  $541 \pm 14$  Ma (He et al. 2016). A layer of coarse-grained calc-  
131 silicate rock and coarse-grained anorthosite occur at the contact of the mineralized zone  
132 (Jayawardena, 1982). The calc-silicate is mainly composed of calcite, apatite and olivine  
133 (fayalite) and the anorthosite is mainly composed of plagioclase with labradorite composition  
134 (Pathirana, 1980). Secondary calc-silicate veins containing sulphides occur along fractures of  
135 the section. Secondary veins containing serpentinite, anhydrite or gypsum are also present  
136 (Jayawardena, 1982).

137 The massive magnetite ore bodies range in thickness from 1–10 meters and consists of  
138 highly coarse-grained magnetite and apatite in which the magnetite contains diopside  
139 inclusions. The disseminated magnetite ores formed within the calc-silicate veins together  
140 with minor sulphides, and are mainly composed of magnetite, chalcopyrite, pyrrhotite, and  
141 pyrite together with apatite and scapolite, tremolite, diopside and minor actinolite and calcite.  
142 The chalcopyrite is better-developed in the disseminated ore compared with the massive ores.

## 143 **PETROLOGY**

144 We summarize below brief field relations and salient petrographic features of the  
145 different rock types from which twelve representative samples were analyzed in this study  
146 (Table 1). The representative field photographs are shown in Fig. 3.

147 The magnetite–apatite ore and host rock samples were collected from a disused mine  
148 in Block-C of the Seruwila deposit. According to the mineral assemblages, the rocks can be  
149 divided into: 1) ultramafic host rock; 2) massive magnetite–apatite ore rock; 3) disseminated  
150 magnetite–apatite ore and 4) transitional zone ore-bearing ultramafic rock and 5)

151 clinopyroxene-bearing enderbite basement rock (He et al. 2016). Neither metamorphic fabric  
152 nor deformational features occur in the studied rocks.

153 **Group 1: ultramafic host rocks.** Sample VC16-1 and VC18-4 represent the ultramafic host  
154 rocks of the magnetite–apatite ore. In hand specimen, the rocks display medium to coarse-  
155 grained texture with clinopyroxene, amphibole, as the dominant minerals with minor fine-  
156 grained magnetite and apatite. The pale green clinopyroxene occurs as medium to coarse-  
157 grained (1–2 mm) euhedral crystals and some carry amphibole inclusions (Fig. 4a). They  
158 show cumulus textures including grain triple junctions and large dihedral angles ( $\sim 120^\circ$ ) (Fig.  
159 4a, b). Texturally two types of amphiboles are identified; the first is represented by coarse-  
160 grained (0.5–1 mm), pale green euhedral amphibole which is free of inclusions. The second  
161 type is fine-grained ( $< 0.1$  mm) and brownish, occurring as anhedral inclusions in  
162 clinopyroxene. The main opaque mineral is magnetite, the distribution of which is limited in  
163 these samples (Fig. 4a), with smaller grain size and irregular morphology compared to the  
164 magnetite crystals in sample VC18-3 and VC18-6. Zircon grains usually occur as inclusions  
165 in the silicate minerals (Fig. 4b).

166 **Group 2: Massive magnetite–apatite ore rocks.** Samples VC18-3, VC16-4 are mainly  
167 composed of coarse-grained magnetite with abundant apatite (Fig. 3a). The mineral  
168 assemblage consists of magnetite (30–40 vol%), apatite (20–30 vol%), amphibole (15–20  
169 vol%) and clinopyroxene (5–10 vol%) with minor spinel. The rock shows a magmatic texture  
170 in the absence of foliation and carries euhedral magnetite with size up to 3–5 cm and coarse-  
171 grained euhedral apatite more than 3 cm in diameter (Fig. 4c, d). Magnetite contains  
172 inclusions of apatite and green euhedral spinel. Spinel usually occurs along magnetite  
173 boundaries and shows hexagonal shape. Euhedral apatite grains are also common as  
174 inclusions in magnetite.

175 **Group 3: Disseminated magnetite–apatite ore rocks.** Samples VC16-2, 18-1 and 18-6 are  
176 apatite-bearing disseminated magnetite ores (Fig. 3b, c). The mineral assemblage is magnetite,  
177 apatite, and scapolite with minor amphibole, clinopyroxene, and calcite. The dominant  
178 amphibole is brownish, coarse-grained (1–2 mm) and subhedral and is interpreted to be the  
179 primary mineral in the protolith (Fig. 4e, f). Clinopyroxene occurs in two textural  
180 associations in both groups of samples: one as coarse greenish grains (size 1–2 mm in size)  
181 and the other as subhedral brownish grains with amphibole rims (Fig. 4f). Brown colored  
182 anhedral actinolite surrounding clinopyroxene (0.2–0.5 mm) may represent a late stage  
183 mineral (Fig. 4e), and the dark brown to red thin band occurring along the boundary of  
184 magnetite and clinopyroxene probably formed during later alteration. The other textural  
185 occurrence of clinopyroxene is as smaller grains mainly surrounded by actinolite, possibly  
186 formed through hydrous alteration. Apatite is white to light gray in color and occurs as  
187 euhedral to subhedral crystals. Apatite also occurs as inclusions within magnetite, and most  
188 apatite grains contain abundant fluid inclusions. Magnetite in disseminated ore samples  
189 shows is characterized by smaller and anhedral grain shapes, and is mostly found surrounding  
190 silicates as aggregates and less in spinel exsolution (Fig. 4d) compared to the massive  
191 magnetite ores. The apatite to magnetite proportion is highly variable. Chalcopyrite occurs as  
192 anhedral grains along with magnetite and scapolite. Most calcite and actinolite occur at the  
193 grain boundary, surrounding magnetite or amphiboles, and are generally anhedral. Scapolite  
194 is characterized by replacement textures cutting across magnetite and silicates (Fig. 4).

195 **Group 4: Transitional zone ore-bearing ultramafic rocks.** Sample VC16-3, 16-5, 16-6,  
196 18-2, 18-5 are from the transitional zone of the ore body and ultramafic rocks (Fig. 3d). They  
197 are generally medium to coarse-grained with equigranular massive texture, and are dark  
198 colored in hand specimen. The rocks are composed of clinopyroxene, magnetite, amphibole,  
199 scapolite, and apatite with accessory hematite. The pale green colored clinopyroxene occurs



200 as subhedral crystals (Fig. 4g, h). Amphibole is fine to medium grained and subhedral, and  
201 the clinopyroxene and amphibole are free of inclusions (Fig. 4g, h). Scapolite is light green in  
202 color, medium to coarse-grained (0.5–1.5 cm) and contains abundant needle-like apatite  
203 inclusions. Apatite not included in scapolite occurs as medium to coarse-grained colorless  
204 crystals (0.5–1.5 cm). Magnetite and minor chalcopyrite are the dominant opaque minerals  
205 with size ranging in size from medium to coarse-grained (1–3 mm) and occur as anhedral  
206 disseminated crystals.

## 207 ANALYTICAL METHODS

208 Mineral chemical analyses were carried out using an electron microprobe analyzer (JEOL  
209 JXA8530F) at the Chemical Analysis Division of the Research Facility Center for Science  
210 and Technology, the University of Tsukuba. Whole-rock major-oxides and trace-elements  
211 including rare earth elements (REE) of sixteen representative samples were analyzed by XRF  
212 and LA–ICP–MS instruments at the National Research Centre of Geoanalyses, Beijing  
213 (China). U–Pb dating and trace element analysis of zircon were simultaneously conducted by  
214 laser ablation–inductively coupled plasma–mass spectrometry (LA–ICP–MS) at the Key  
215 Laboratory of Continental Collision and Plateau Uplift, Institute of Tibetan Plateau Research,  
216 Chinese Academy of Science, Beijing, China. In situ zircon Hf isotopic analyses were  
217 conducted on the same spots or in the adjacent domains where U–Pb dating was done.  
218 The details of analytical techniques relating to petrography, mineral chemistry, whole rock  
219 chemistry, and zircon U–Pb and Lu–Hf isotopic analyses are given in Supplementary file:  
220 Appendix 1.

## 221 RESULTS

222 The details of mineral chemistry, whole rock chemistry, zircon U–Pb and Lu–Hf isotopic  
223 analyses results are given in Supplementary file: Appendix 1. The related figures are Figs. 5–

224 9. The data table are in Table 2 and Supplementary Table 1–3.

## 225 **DISCUSSION**

### 226 **Petrogenesis of Seruwila ultramafics: a CO<sub>2</sub> and LREE enriched** 227 **metasomatized mantle beneath VC–HC boundary?**

228 The ultramafic samples (clinopyroxenite) are distinct from the surrounding  
229 Neoproterozoic (ca. 924 Ma, He et al. 2016) granitic basement rocks which are strongly  
230 deformed and metamorphosed at upper amphibolite- to granulite-facies conditions. Neither  
231 metamorphic fabric nor deformational features are observed in the ultramafic host or their  
232 ore-bearing zones (Fig. 3). The close relationship of the ultramafics with ore deposit,  
233 particularly the massive ores which occur within the ultramafic rock suggests a genetic link  
234 between the ultramafic rocks and the mineralization. The high-Mg bulk chemistry, cumulus  
235 texture including grain triple junctions and the large dihedral angle (~120°, Fig. 4a, b)  
236 (Holness et al. 2005), the coarse-grained euhedral crystal shape of pyroxene and amphibole,  
237 and the association of anorthosite in this deposit (Jayawardena, 1982) suggest fractionation in  
238 a volatile-rich magma chamber. Apatite chemistry characterized by moderately high  
239 concentration of F and Cl further support the volatile-rich signature (Fig. 5b).

240 All the studied samples are characterized by low silica, high Mg, Fe, Ca and a narrow  
241 range in Sm/Nd ratios consistently less than the bulk Earth value. They show general HFSE  
242 depletion including negative Zr, Hf, Ti, Y anomalies (Fig. 6). The chondrite-normalized REE  
243 compositions and primitive-mantle-normalized trace element compositions (Fig. 6) are  
244 characterized by LREE enrichment with variable total LREE concentrations and HREE  
245 depletion. Jayawardena (1982) analyzed the bulk chemistry of the adjacent calc-silicates and  
246 reported very low values of metallic elements as compared to those in the massive and  
247 disseminated ores. However, the calc-silicate rocks show comparatively high manganese

248 concentrations (437–754 ppm) and high Y, La, Sr and Ba contents. The calc-silicate rock was  
249 likely the source for the late-stage calcic metasomatism (scapolitization and actinolitization)  
250 and probably was not the major source of Fe in the ore deposit.

251         The combined petrological and geochemical features suggest that the ultramafics in  
252 Seruwila represent the cumulate phase of a highly fractionated volatile-rich magma. The  
253 depleted HREE contents indicates that the primitive magma was likely generated from deep  
254 level, where the residual phases are dominated by garnet rather than plagioclase or spinel.  
255 The enrichment of LREE, high contents of volatiles and the low SiO<sub>2</sub>, Cr, Ni, and low Sm/Nd  
256 ratios indicate that the Seruwila ultramafics were derived from an enriched mantle source  
257 region beneath VC–HC boundary. This boundary extends SW from Seruwila towards  
258 Dehiattakandiya, east of the Mahaweli and up to Buttala where several serpentinite and  
259 magnetite deposits have been identified. Along its southeast extension, Ni and Cr bearing  
260 serpentinites have also been detected. He et al. (2016) carried out a detailed study on the  
261 serpentinites and reported abundant magnesite veins and pods suggesting CO<sub>2</sub>-induced  
262 mantle metasomatism in the mantle wedge. We thus interpret that the Seruwila ultramafics  
263 were likely derived from a CO<sub>2</sub> and LREE enriched metasomatized mantle. This  
264 interpretation is consistent with experimental data that CO<sub>2</sub>-rich vapor is a suitable  
265 transporting medium for LREE, iron and P (Harrison 1979).

## 266 **Age data implications**

267         Zircon grains from the transition zone sample VC16-3 and ultramafic host rock sample  
268 VC18-4 are mostly homogeneous without clear core-rim texture (Fig. 7) and they yield  
269 <sup>206</sup>Pb/<sup>238</sup>U age of 527 ± 3 Ma and 530 ± 4 Ma, respectively (Fig. 8). However, the  
270 interpretation of these ages is not straight forward because most ultramafic rocks are highly  
271 Zr-unsaturated (< 50 ppm Zr) and Si-poor (Erlank et al. 1978). Thus, zircon seldom

272 crystallizes from ultramafic magma because of less silica activity and low Zr content  
273 (Heaman et al. 1990; Finch and Hanchar 2003; Wang et al. 2016 and references there in).

274 In spite of the common Zr-depleted compositions for ultramafic rocks, the occurrence of  
275 zircon grains have been reported from several localities including metasomatized peridotites  
276 from the Kokchetav Massif, Kazakhstan (e.g., Katayama et al. 2003), serpentinites and  
277 rodingites within serpentinized mantle peridotites (Tsuji-mori et al. 2005) and garnet peridotite  
278 (Liati et al. 2004). This suggests that metasomatic fluids can contribute additional Zr to the  
279 generally Zr-poor lithospheric mantle, thereby enriching mafic/ultramafic melts derived from  
280 such sources. Also, the higher Zr content in the rocks of present study (135–372 ppm)  
281 compared to typical gabbroic rocks (Erlank et al. 1978) and the presence of zircon grains as  
282 inclusions in euhedral clinopyroxene suggest a magmatic origin. Furthermore, the relatively  
283 anhedral zircon crystal with patchy zoning is also typical of zircon grains in ultramafic rocks  
284 (Fig. 7) (Grieco et al. 2001; Corfu et al. 2003; Zheng et al. 2006; Lei et al. 2016). Their high  
285 Th/U ratios further support this interpretation as Th is usually depleted in hydrothermal fluid.  
286 Therefore, these two identical ages and are taken to represent the emplacement timing of the  
287 ultramafic intrusion during Early Cambrian. This age is younger than the timing of regional  
288 high-grade metamorphism reported in this area (580–540 Ma) (Widanagamage 2011; Kröner  
289 et al. 2013; He et al. 2016; Ng et al. 2017).

290 The zircon Lu–Hf data from both samples show  $\epsilon\text{Hf}(t)$  values around zero and plot on the  
291 CHUR line (Fig. 9). The tight ( $^{176}\text{Hf}/^{177}\text{Hf}$ )<sub>i</sub> range of 0.282339 to 0.282482 indicates that the  
292 zircon Lu–Hf systematics is unlikely to have been modified by later stage fluid. The two-  
293 stage Hf model ages ( $T_{\text{DM}}$ ) varies from 1263 to 1064 Ma, suggesting melt derived from late  
294 Mesoproterozoic to early Neoproterozoic depleted mantle with no or limited crustal  
295 contamination.

296 In summary, the 530 Ma ages of the ultramafics from the Seruwila area on the VC–HC

297 boundary is younger than the age of high-grade metamorphism associated with the  
298 amalgamation of the Wannan and Vijayan Complex during Gondwana assembly. Therefore, the  
299 530 Ma is likely to represent a post-collisional ultramafic magmatism during early Cambrian  
300 triggered by lithospheric extension.

## 301 **Implications**

### 302 Kiruna-type associated with ultramafics

303 Iron oxide–apatite (IOA) deposits occur within a variety of host rocks and tectonic  
304 settings. Nelsonites (Fe–Ti oxide apatite rock) and Kiruna-type iron oxide–apatite rocks are  
305 the two typical varieties. Nelsonites usually form massive Fe–Ti oxide ore deposits within  
306 anorthosites (Owens and Dymek 1992). They have been interpreted by some as the product  
307 of liquid (rich in Ti, P, ± Zr) immiscibility from magmas of ferrodioritic composition  
308 (Philpotts 1967, 1981; Watson and Green 1981; Ashwal 1993; Darling and Florence 1995),  
309 or as cumulate zones within oxide ores (locally mobilized as dike like bodies), although their  
310 host Fe–Ti oxide ores may represent immiscible oxide liquids (Owens and Dymek 1992;  
311 Dymek and Owens 1996, 2001). Geological, textural, mineralogical, and geochemical data  
312 collectively indicate that the magnetite–apatite association in the Seruwila area differs from  
313 typical nelsonite in terms of the nature of the host rock, the Ti-poor compositions of  
314 magnetite, the highly variable proportion of apatite and magnetite with presence of silicates,  
315 and the significant REE fractionation in all the samples (Dymek and Owens 2001).

316 The Kiruna-type IOA rocks contain variable quantities of magnetite–apatite mostly  
317 related to intermediate alkaline or calc-alkaline rocks (Hilderband, 1986, Nyström and  
318 Henriquez, 1994). Typical examples include the Kiruna deposit in Sweden (e.g. Jonsson et al.  
319 2013), the El Laco deposit in Chile (e.g. Dare et al. 2015), and Bafq area in Iran (Sabet-  
320 Mobarhan-Talab et al. 2015). Rare examples of Kiruna-type mineralization associated with

321 mafic/ultramafic intrusions have been reported in the Upper Zone of the Bushveld Complex  
322 where the IOA deposit is hosted in layered mafic intrusions (Von Gruenewaldt 1994), in  
323 Georgia and Maryland of the USA associated with chlorite–talc schists located in ultramafic  
324 bodies (Herz and Valentine 1970), in Lizard Ophiolite Complex, UK related to Fe–Ti oxide-  
325 rich gabbro (Hopkinson and Roberts 1995) and in Orthys Ophiolite Complex, Greece  
326 associated with peridotite (plagioclase lherzolite) (Mitsis and Economou-Eliopoulos 2001).  
327 The Kiruna-type IOA deposits are generally attributed to extensional sub-domains such as  
328 rifts and/or back-arcs in active convergent (Andean-type) continental margins, and to  
329 intracontinental (intracratonic) rifts within a subaerial to shallow marine basinal sequences  
330 floored by crystalline basement (Hilderband 1986; Nyström and Henriquez, 1994; Jonsson et  
331 al. 2013; Taghipour et al. 2015; Knipping et al. 2015). However, the origin of Kiruna-type  
332 rocks remains equivocal. Some researchers favor a magmatic origin (Naslund et al. 1998;  
333 Jonsson et al. 2013) and others a hydrothermal origin (Barton and Johnson 1996; Dare et al.  
334 2015; Sabet-Mobarhan-Talab et al. 2015). Recent studies propose an integrated model of  
335 magmatic–hydrothermal system for the Kiruna-type mineralization (Jonsson et al. 2013;  
336 Taghipour et al. 2015; Knipping et al. 2015), providing new insights on the genesis of  
337 Kiruna-type IOA deposit, and suggesting a genetic relation with iron-oxide–copper–gold  
338 (IOCG) deposits.

339 The iron oxide–apatite deposit at Seruwila shows many similarities with the Kiruna-type  
340 iron oxide apatite deposits, particularly with respect to the mineral assemblages, structure of  
341 the iron ores, and chemical composition of ore minerals and occurrence of the alteration  
342 zones. However, it differs from other IOA deposit hosted in mafic/ultramafic host rocks  
343 including the examples mentioned above. In all of these cases, only small apatite crystals are  
344 associated with Fe–Ti oxides. The lack of Ti-oxides (ilmenite, rutile) is also a major  
345 difference. In the present case, the large magnetite with chlor-fluorapatite crystals hosted in

346 an ultramafic body along a major tectonic boundary, with nearly end-member composition of  
347 magnetite and distinct REE-enrichment may suggest a new type of IOA association  
348 developed within a post collisional tectonic setting. This is probably the first report of a  
349 Kiruna-type IOA deposit associated with ultramafics within a suture system. Our study  
350 suggests significant potential for the occurrence of similar deposits elsewhere in the  
351 Gondwana suture systems.

### 352 The genesis of iron mineralization: magmatic or hydrothermal?

353 The close spatial relation, similarity of the trace element signatures, REE distribution patterns  
354 and zircon Lu–Hf isotopic data of all studied samples indicate that the Seruwila iron oxide–  
355 apatite ore and host ultramafic are genetically related. The fluorine-rich nature of apatite  
356 indicates contributions from a volatile-enriched magma. However, depletion in elements  
357 considered relatively immobile in hydrothermal fluids (such as Ti, Al, Cr, Zr, Hf and Y)  
358 suggests the involvement of hydrothermal processes. We interpret the genesis of Seruwila  
359 deposit reflecting both magmatic and hydrothermal processes (also termed as “ortho-  
360 magmatic”). The presence of Ca-rich scapolite and actinolite replacement textures indicate a  
361 late-stage calcic metasomatism, as also does the occurrence of calc-silicate layers/veins  
362 within the ore-bearing rocks. The composition of scapolite is Cl-bearing Meionite (Ca-rich),  
363 and previous workers have suggested that scapolites associated with the carbonate  
364 metasomatism tend towards the meionitic (CaCO<sub>3</sub>-rich) end-member (e.g. Pan, 1998; Shaw,  
365 1960a). Therefore, we interpret that scapolite formed by calcic metasomatism through  
366 interaction with the surrounding calc-silicate rocks.

367 The lithologic and petrological features of the Seruwila IOA deposit point to two  
368 different stages of mineralization: 1) the massive magnetite–apatite mineralization; and 2) the  
369 disseminated magnetite–apatite–copper sulfide mineralization. The massive magnetite ore  
370 samples are characterized by coarse-grained euhedral pure magnetite with ubiquitous spinel

371 exsolution and cumulus textures, whereas the apatite occurs as coarse euhedral crystals free  
372 of inclusions, consistent with high T environment. In contrast, the disseminated magnetite ore  
373 samples are mostly composed of subhedral to anhedral magnetite with little spinel exsolution  
374 but commonly containing silicate mineral aggregates, and the associated apatite is finer-  
375 grained with abundant fluid-inclusions indicating that the disseminated mineralization formed  
376 after the massive-type magnetite at a lower temperature. The high Al and low Cr contents of  
377 spinel, and the low Ti, Al, and Mn of magnetite exclude formation from a pure magmatic  
378 melt derived from peridotitic mantle (e.g., Kubo, 2002). Instead, the involvement of high  
379 temperature fluids exsolved from the ultramafic magma is suggested. Therefore, we interpret  
380 a high-T “magmatic–hydrothermal” origin for the massive type magnetite and a low-T  
381 hydrothermal origin for the disseminated magnetite.

382 Knipping et al. (2015) proposed that metals preferred wetting of magnetite in a Cl-  
383 bearing magmatic-hydrothermal system, causing buoyant segregation of the magnetite  
384 suspension as chloride complexes. Experimental data suggest that Ca, water and volatiles (F,  
385 Cl, P) strongly fractionate into the iron-rich melt (Simon et al. 2004; Bell and Simon, 2011).  
386 This model is consistent with our data as indicated by the highest Cl content in apatite and  
387 magnetite in massive type ore samples and lowest in ultramafic host samples, which could  
388 also result from seawater recycling of the subducted slab (Philippot et al. 1998). In terms of  
389 the minor Cu-bearing sulfide minerals occurring with disseminated magnetite, it has been  
390 commonly observed that the precipitation of sulfide-oxide usually happens near-surface or at  
391 shallow level due to the physicochemical changes within the hydrothermal system (Foose et  
392 al. 1985; Scott et al. 1990; Eliopoulos et al. 1998).

393 Based on the evidence presented in our study, we propose a two-stage model for the  
394 mineralization of Seruwila IOA deposit as follows (Fig. 10). 1) The Cl-rich magmatic–  
395 hydrothermal fluid scavenged iron and P from the ultramafic magma, transported iron as



396 magnetite suspensions and ascended due to positive buoyancy. With the sudden decrease of  
397 pressure and temperature in the post-collision extensional setting after the collision of VC  
398 and HC, magnetite suspensions accumulated to form the massive type magnetite with  
399 abundant apatite. 2) Progressive cooling and ascending caused the eventual growth of  
400 disseminated magnetite and the precipitation of sulfide mineral at shallower level and trapped  
401 abundant fluid-inclusions aided by hydrothermal fluid at shallower depth, forming the  
402 disseminated ore body, followed by calcic metasomatism (scapolitization and actinolitization)  
403 possibly through interaction with the proximal carbonate rocks.

## 404 **ACKNOWLEDGEMENTS**

405 We thank the editors Dr. Julie Roberge and Dr. Keith Putirka from American Mineralogist, as  
406 well as three anonymous referees for their constructive comments and suggestions which  
407 greatly helped in improving our paper. We also thank Prof. Martin Hand for his valuable  
408 corrections. Funding for this study was provided by Toshiaki Tsunogae through a Grant-in-  
409 Aid for Scientific Research (B) from Japan Society for the Promotion of Science (JSPS)  
410 (Grant No. 26302009) and the Fundamental Research Funds for the Central Universities (No.  
411 2652017002). The study was also funded by M. Santosh from the Foreign Expert funds from  
412 the China University of Geosciences Beijing, China and Professorial position at the  
413 University of Adelaide, Australia. This study forms part of Xiao-Fang He's doctoral research  
414 at the China University of Geosciences Beijing and at the University of Adelaide, Australia,  
415 supported by the Chinese Scholarship Council (CSC).

## 416 **REFERENCES CITED**

417 Ashwal, L. D., Hamilton, M. A., Morel, V. P., and Rambeloson, R. A. (1998) Geology,  
418 petrology and isotope geochemistry of massif-type anorthosites from southwest  
419 Madagascar. *Contributions to Mineralogy and Petrology*, 133(4), 389–401.

- 
- 420 Barton, M. D., and Johnson, D. A. (1996) Evaporitic-source model for igneous-related Fe  
421 oxide–(REE-Cu-Au-U) mineralization. *Geology*, 24(3), 259–262.
- 422 Bell, A. S., and Simon, A. (2011) Experimental evidence for the alteration of the  $\text{Fe}^{3+}/\Sigma\text{Fe}$  of  
423 silicate melt caused by the degassing of chlorine-bearing aqueous volatiles. *Geology*,  
424 39(5), 499–502.
- 425 Blichert-Toft, J., and Albarède, F. (1998) The Lu–Hf isotope geochemistry of chondrites and  
426 the evolution of the mantle–crust system. *Earth and Planetary Science Letters*, 154, 349.
- 427 Braun, I., and Kriegsman, L. M. (2003). Proterozoic crustal evolution of southernmost India  
428 and Sri Lanka. Geological Society, London, Special Publications, 206(1), 169–202.
- 429 Brooks, R.R., Baker, A.J.M., Ramakrishna, R.S., and Ryan, D.E. (1985) Botanical and  
430 geochemical exploration studies at the seruwila copper-magnetite prospect in Sri Lanka.  
431 *Journal of Geochemical Exploration*, 24, 223–235.
- 432 Chu, N.C., Taylor, R.N., Chavagnac, V., Nesbitt, R.W., Boella, R.M., Milton, J.A., Germain,  
433 C.R., Bayon, G., and Burton, K. (2002) Hf isotope ratio analysis using multi-collector  
434 inductively coupled plasma mass spectrometry: an evaluation of isobaric interference  
435 corrections. *Journal of Analytical Atomic Spectrometry*, 17, 1567–1574.
- 436 Cooray, P.G. (1994) The Precambrian of Sri Lanka: a historic review. *Precambrian Research* 66,  
437 3-18.
- 438 Corfu, F., Hanchar, J.M., Hoskin, P.W.O., and Kinny, P. (2003) Atlas of Zircon Textures.  
439 Zircon: Mineralogical Society of America Reviews in Mineralogy and Geochemistry, 53,  
440 469–500.
- 441 Dare, S.A.S., Barnes, S., and Beaudoin, G. (2015) Did the massive magnetite ‘lava flows’ of El  
442 Laco (Chile) form by magmatic or hydrothermal processes? New constraints from  
443 magnetite composition by LA-ICP-MS. *Mineralium Deposita*, 50, 607–617.

- 
- 444 Darling, R. S., and Florence, F. P. (1995) Apatite light rare earth element chemistry of the Port  
445 Leyden nelsonite, Adirondack Highlands, New York; implications for the origin of  
446 nelsonite in anorthosite suite rocks. *Economic Geology*, 90(4), 964–968.
- 447 Dissanayake, C.B., and Van Riel, B.J. (1978) Petrology and geochemistry of a recently  
448 discovered nickeliferous serpentinite in Sri Lanka. *Geological Society of India*, 19(10),  
449 464–471.
- 450 Dissanayake, C.B., and Weerasooriya, S.V.R. (1986) Fluorine as an indicator of mineralization  
451 - Hydrogeochemistry of a Precambrian mineralized belt in Sri Lanka. *Chemical Geology*,  
452 56, 257–270.
- 453 Dharmapriya, P.L., Malaviarachchi, S.P.K., Santosh, M., Tang, L., and Sajeev, K. (2015) Late-  
454 Neoproterozoic ultrahigh temperature metamorphism in the Highland Complex, Sri  
455 Lanka. *Precambrian Research* 271, 311–333.
- 456 Dymek, R. F., and Owens, B. E. (1996) Petrogenetic relationships among FTP-rocks of the  
457 anorthosite suite (nelsonites, OAGNs, jotunites, and oxide ores) as revealed by REE  
458 characteristics of separated apatites. Geological Society of America. In Abstracts with  
459 Program (Vol. 28, p. 288)
- 460 Dymek, R. F., and Owens, B. E. (2001) Petrogenesis of apatite-rich rocks (nelsonites and  
461 oxide-apatite gabbro-norites) associated with massif anorthosites. *Economic  
462 Geology*, 96(4), 797-815.
- 463 Eliopoulos, D., Skounakis, S., and Economou-Eliopoulos, M. (1998) Geochemical  
464 characteristics of sulfide mineralizations from the Pindos ophiolite complex. *Bulletin of  
465 the Geological Society of Greece*, XXXII, No 3, 179–186.
- 466 Erlank, A. J., Smith, A. S., Marchant, J. W., Cardoso, M. P., and Ahrens, L. H. (1978) Zr, in  
467 Wedepohl, K. H., ed., *Handbook of geochemistry*, v. II-4, section 40: New York, NY,  
468 Springer.

- 
- 469 Finch, R. J., and Hanchar, J. M. (2003) Structure and chemistry of zircon and zircon-group  
470 minerals. *Reviews in mineralogy and geochemistry*, 53(1), 1–25.
- 471 Foose, M. P., and McLelland, J. M. (1995) Proterozoic low-Ti iron-oxide deposits in New York  
472 and New Jersey: Relation to Fe-oxide (Cu–U–Au–rare earth element) deposits and  
473 tectonic implications. *Geology*, 23(7), 665–668.
- 474 Grieco, G., Ferrario, A., Von Quadt, A., Koepfel, V., and Mathez, E.A. (2001) The Zircon-  
475 Bearing Chromitites of the Phlogopite Peridotite of Finero (Ivrea Zone, Southern Alps):  
476 Evidence and Geochronology of a Metasomatized Mantle Slab. *Journal of Petrology*, 42,  
477 89–101.
- 478 Griffin, W.L., Pearson, N.J., Belousova, E., Jackson, S.E., Van Achenbergh, E., O'Reilly, S.Y.,  
479 and Shee, S.R. (2000) The Hf isotope composition of cratonic mantle: LAM-MC-ICPMS  
480 analysis of zircon megacrysts in kimberlites. *Geochimica et Cosmochimica Acta*, 64,  
481 133–147.
- 482 Griffin, W.L., Belousova, E.A., Shee, S.R., Pearson, N.J., and O'Reilly, S.Y. (2004) Archean  
483 crustal evolution in the northern Yilgarn Craton: U-Pb and Hf-isotope evidence from  
484 detrital zircons. *Precambrian Research*, 131, 231–282.
- 485 Harrison, W. J. (1979) Partitioning of REE between garnet peridotite minerals and coexisting  
486 melts during partial melting. *Carnegie Inst. Washington Yearbk*, 78, 562-568.
- 487 He, X.F., Santosh, M., Tsunogae, T., Malaviarachchi, S.P.K., and Dharmapriya, P.L., (2016)  
488 Neoproterozoic arc accretion along the “eastern suture” in Sri Lanka during Gondwana  
489 assembly. *Precambrian Res.* 279, 57–80. doi:10.1016/j.precamres.2016.04.006.
- 490 Heaman, L. M., Bowins, R., and Crocket, J. (1990). The chemical composition of igneous  
491 zircon suites: implications for geochemical tracer studies. *Geochimica et Cosmochimica*  
492 *Acta*, 54(6), 1597–1607.

- 
- 493 Henriquez, F., and Martin, R. F. (1978) Crystal-growth textures in magnetite flows and feeder  
494 dykes, EL Laco, Chile: *Canadian Mineralogist* 16, 581–589.
- 495 Herz, N., and Valetine, L.B. (1970) Rutile in the Harford Country, Maryland, serpentine belt.  
496 U.S. Geological Survey Professional Paper 700-C, 43–48.
- 497 Hilderband, R.S. (1986) Kiruna-type deposits: Their origin and relationship to intermediate  
498 subvolcanic plutons in the Great Bear magmatic zone, Northwest Canada. *Economic*  
499 *Geology*, 8, 640–659.
- 500 Hitzman, M. W., Oreskes, N., and Einaudi, M. T. (1992) Geological characteristics and tectonic  
501 setting of proterozoic iron oxide (Cu □ U □ Au □ REE) deposits. *Precambrian*  
502 *Research*, 58(1-4), 241–287.
- 503 Holness, M.B., Cheadle, M.J., and Kenzie, D.A.N.M.C. (2005) On the Use of Changes in  
504 Dihedral Angle to Decode Late-stage Textural Evolution in Cumulates. *Journal of*  
505 *Petrology*, 46, 1565–1583.
- 506 Hopkinson, L., and Roberts, S. (1995) Ridge axis deformation and coeval melt migration within  
507 layer 3 gabbros: evidence from the Lizard complex, U.K. *Contributions to Mineralogy*  
508 *and Petrology* 121, 126–138.
- 509 Horstwood, M.S.A., Košler, J., Gehrels, G., Jackson, S.E., Mclean, N.M., Paton, C., Pearson,  
510 N.J., Sircombe, K., Sylvester, P., Vermeesch, P., and others (2016) Community-Derived  
511 Standards for LA-ICP-MS U-(Th-)Pb Geochronology - Uncertainty Propagation, Age  
512 Interpretation and Data Reporting. *Geostandards and Geoanalytical Research*, 40, 311–  
513 332.
- 514 Hou, T., Zhang, Z., Encarnacion, J., Huang, H., and Wang, M. (2012)  
515 Geochronology/geochemistry of the Washan dioritic porphyry associated with Kiruna-  
516 type iron ores, Middle-Lower Yangtze River Valley, eastern China: implications for  
517 petrogenesis/mineralization. *International Geology Review*, 54, 1332–1352.

- 518 Jaffey, A.H., Flynn, K.F., Glendenin, L.E., Bentley, W.C., and Essling, A.M. (1971) Precision  
519 measurement of half-lives and specific activities of  $^{235}\text{U}$  and  $^{238}\text{U}$ . *Physical Review C*, 4,  
520 1889–1906.
- 521 Jayawardena, D.E. d. S. (1982) The Geology and Tectonic Setting of the Copper-Iron Ore  
522 Prospect at Seruwila - North East Sri Lanka. *Journal of the National Science Council of*  
523 *Sri Lanka*, 10, 129–142.
- 524 Jonsson, E., Troll, V.R., Högdahl, K., Harris, C., Weis, F., Nilsson, K.P., and Skelton, A. (2013)  
525 Magmatic origin of giant ‘Kiruna-type’ apatite-iron-oxide ores in central Sweden.  
526 *Scientific reports*, 3, 1644.
- 527 Katayama, I., Mukou, A., Iizuka, T., Maruyam, S., Terada, K., Tsutsumi, Y., Sano, Y., Zhang,  
528 R.Y., and Liou, J.G., 2003. Dating of zircon from Ti-clinohumite-bearing garnet  
529 peridotite: implication for timing of mantle metasomatism. *Geology* 31, 713–716.
- 530 Knipping, J.L., Bilenker, L.D., Simon, A.C., Reich, M., Barra, F., Deditius, A.P., Lundstrom,  
531 C., Bindeman, I., and Munizaga, R. (2015) Giant Kiruna-type deposits form by efficient  
532 flotation of magmatic magnetite suspensions. *Geology*, 43, 591–594.
- 533 Kröner, A., Cooray, P. G., and Vitanage, P.W. (1991) Lithotectonic subdivision of the  
534 Precambrian basement in Sri Lanka. Geological Survey Department, Sri Lanka,  
535 Professional Paper 5, 5-21.
- 536 Kröner, A., Rojas-Agramonte, Y., Kehelpannala, K.V.W., Zack, T., Hegner, E., Geng, H.Y.,  
537 Wong, J., and Barth, M. (2013) Age, Nd–Hf isotopes, and geochemistry of the Vijayan  
538 Complex of eastern and southern Sri Lanka: a Grenville-age magmatic arc of unknown  
539 derivation. *Precambrian Research* 234, 288–321.
- 540 Kubo, T., Ohtani, E., Kondo, T., and Kato, T. (2002) Metastable garnet in oceanic crust at the  
541 top of the lower mantle. *Nature*, 420(6917), 803.

- 
- 542 Leake, B.E., Woolley, A.R., Arps, C.E., Birch, W.D., Gilbert, M.C., Grice, J.D., Hawthorne,  
543 F.C., Kato, A., Kisch, H.J., Krivovichev, V.G., and Linthout, K. (1997) Nomenclature of  
544 Amphiboles: Report of the Subcommittee on Amphiboles of the International  
545 Mineralogical Association Commission on New Minerals and Mineral Names. Mineral.  
546 Mag. 61, 295–321.
- 547 Lei, W., Shi, G., Santosh, M., Ng, Y., Liu, Y., Wang, J., Xie, G., and Ju, Y. (2016) Trace  
548 element features of hydrothermal and inherited igneous zircon grains in mantle wedge  
549 environment: A case study from the Myanmar jadeitite. *Lithos*, 266–267, 16–27.
- 550 Liati, A., Franz, L., Gebauer, D., and Fanning, C.M. (2004) The timing of mantle and crustal  
551 events in South Namibia, as defined by SHRIMP-dating of zircon domains from a garnet  
552 peridotite xenolith of the Gibeon Kimberlite Province. *Journal of African Earth*  
553 *Sciences*, 39(3), 147–157.
- 554 Ludwig, K. R. (2012) ISOPLOT 3.75: A Geochronological Toolkit for Microsoft Excel.  
555 Berkeley Geochronology Centre, Special Publication, 1–75.
- 556 McDonough, W.F., and Sun, S.S. (1995) The composition of the Earth. *Chemical Geology* 120,  
557 223–253.
- 558 Milisenda, C.C., Liwa, T.C., Hofmanna, A.W., and Köhler, H. (1994) Nd isotopic mapping of  
559 the Sri Lanka basement: update, and additional constraints from Sr isotopes. *Precambrian*  
560 *Research*, 66, 95–110.
- 561 Mitsis, I., and Economou-Eliopoulos, M. (2001) Occurrence of apatite associated with  
562 magnetite in an ophiolite complex (Othrys), Greece. *American Mineralogist*, 86, 1143–  
563 1150.
- 564 Morimoto, N. (1988) Nomenclature of Pyroxenes. *American Mineralogist* 73, 1123–1133.
- 565 Murray, J.R., and Oreskes, N. (1997) Uses and limitations of cathodoluminescence in the study  
566 of apatite paragenesis. *Economic Geology*, 92, 368–376.

- 
- 567 Naslund, H.R., Dobbs, F.M., Henriquz, F.J., and Nystrom, J.O. (1998) Evidence for iron-oxide  
568 magmas at El Laco, Chile. Geological Society of America Abstracts with Programs 30,  
569 91.
- 570 Ng, S.W.-P., Whitehouse, M.J., Tam, T.P.-Y., Jayasingha, P., Wong, J.P.-M., Denyszyn, S.W.,  
571 Yiu, J.S.-Y., and Chang, S.-C. (2017) Ca. 820–640 Ma SIMS U-Pb age signal in the  
572 peripheral Vijayan Complex, Sri Lanka: Identifying magmatic pulses in the assembly of  
573 Gondwana. *Precambrian Research*, 294, 244–256.
- 574 Nyström, J.O., and Henriquez, F. (1994) Magmatic features of iron ores of the Kiruna-type in  
575 Chile and Sweden: ore textures and magnetite geochemistry. *Economic Geology*, 89,  
576 820–839.
- 577 Owens, B. E., and Dymek, R. F. (1992) Fe–Ti–P-rich rocks and massif anorthosite; problems of  
578 interpretation illustrated from the Labrieville and St-Urbain plutons, Quebec. *The*  
579 *Canadian Mineralogist*, 30(1), 163–190.
- 580 Pan, Y. (1998) Scapolite in skarn deposits: petrogenetic and geochemical significance.  
581 *Mineralized Intrusion-related Skarn Systems*. Mineralogical Association of Canada Short  
582 Course Series, 26, 169–209.
- 583 Park, C.F., Jr. (1961) A magnetite “flow” in northern Chile: *Economic Geology and the*  
584 *Bulletin of the Society of Economic Geologists* 56, 431–436.
- 585 Pathirana, H.D.N.C. (1980) Geology of Sri Lanka in relation to plate tectonics. *Journal of the*  
586 *National Science Council of Sri Lanka* 8(1), 75–85.
- 587 Philippot, P., Agrinier, P., and Scambelluri, M. (1998) Chlorine cycling during subduction of  
588 altered oceanic crust. *Earth and Planetary Science Letters*, 161(1), 33–44.
- 589 Philpotts, A. R. (1967) Origin of certain iron-titanium oxide and apatite rocks. *Economic*  
590 *Geology*, 62(3), 303–315.



- 
- 591 Philpotts, A. R. (1981) A model for the generation of massif-type anorthosites. Canadian  
592 Mineralogist, 19, 233–253.
- 593 Rajapaksha, A.U., Vithanage, M., Oze, C., Bandara, W.M.A.T., and Weerasooriya, R. (2012)  
594 Nickel and manganese release in serpentine soil from the Ussangoda Ultramafic Complex,  
595 Sri Lanka. Geoderma, 189–190, 1–9.
- 596 Sabet-Mobarhan-Talab, A., Alinia, F., Ghannadpour, S.S., and Hezarkhani, A. (2015) Geology,  
597 geochemistry, and some genetic discussion of the Chador-Malu iron oxide-apatite deposit,  
598 Bafq District, Central Iran. Arabian Journal of Geosciences, 8, 8399–8418.
- 599 Santosh, M., Tsunogae, T., Malaviarachchi, Sanjeewa P.K., Zhang, Z.M., Ding, H.X., Tang, L.,  
600 and Dharmapriya, P.L. (2014) Neoproterozoic crustal evolution in Sri Lanka: Insights  
601 from petrologic, geochemical and zircon U–Pb and Lu–Hf isotopic data and implications  
602 for Gondwana assembly. Precambrian Research 255, 1–29.
- 603 Scherer, E. (2001) Calibration of the Lutetium-Hafnium Clock. Science, 293, 683–687.
- 604 Scott, S.D., Chase, M.D., Hannington, P.J., McConachy, T.F., and Shea, G.T. (1990) Sulfide  
605 deposits, tectonics and petrogenesis of Southern, Explorer Ridge, NE Pacific ocean. In  
606 Malpas, J., Moores, E.M., Panayotou, A., and Xenophodos, C. (eds). Proceedings of the  
607 International Symposium on Ophiolites, Oceanic Crustal Evolution, Nicosia, 719–733.
- 608 Seneviratne, S. (1998) The Ecology and Archaeology of the Seruwila Copper-Magnetite  
609 Deposit, North East Sri Lanka. Archaeometall. India 3, 156–175.
- 610 Shaw, D.M. (1960) The geochemistry of scapolite part I. Previous work and general mineralogy.  
611 Journal of Petrology, 1(1), 218–260.
- 612 Sillitoe, R.H., 2003. Iron oxide–copper–gold deposits: an Andean view. Mineral Deposits 38,  
613 787–812.

- 614 Simon, A. C., Pettke, T., Candela, P. A., Piccoli, P. M., and Heinrich, C. A. (2004) Magnetite  
615 solubility and iron transport in magmatic-hydrothermal environments. *Geochimica et*  
616 *Cosmochimica Acta*, 68(23), 4905–4914.
- 617 Sláma, J., Košler, J., Condon, D.J., Crowley, J.L., Gerdes, A., Hanchar, J.M., Horstwood,  
618 M.S.A., Morris, G.A., Nasdala, L., Norberg, N., and others (2008) Plešovice zircon—A  
619 new natural reference material for U-Pb and Hf isotopic microanalysis. *Chemical*  
620 *Geology*, 249, 1–35.
- 621 Söderlund, U., Patchett, P.J., Vervoort, J.D., and Isachsen, C.E. (2004) The  $^{176}\text{Lu}$  decay  
622 constant determined by Lu-Hf and U-Pb isotope systematics of Precambrian mafic  
623 intrusions. *Earth and Planetary Science Letters*, 219, 311–324.
- 624 Sun, S. -s., and McDonough, W.F. (1989) Chemical and isotopic systematics of oceanic basalts:  
625 implications for mantle composition and processes. Geological Society, London, Special  
626 Publications, 42, 313–345.
- 627 Taghipour, S., Kananian, A., Harlov, D., and Oberhänsli, R. (2015) Kiruna-type iron oxide-  
628 apatite deposits, Bafq District, Central Iran: Fluid-aided genesis of fluorapatite-monazite-  
629 xenotime assemblages. *Canadian Mineralogist*, 53, 479–496.
- 630 Takamura, Y., Tsunogae, T., Santosh, M., Malaviarachchi, S.P.K., and Tsutsumi, Y. (2015) U-  
631 Pb geochronology of detrital zircon in Sri Lanka: Implications for the regional correlation  
632 of Gondwana fragments. International Association for Gondwana Research Conference  
633 Series 21, 106–107.
- 634 Tornos, F., Velasco, F., Hanchar, J.M., Astrobiología, C. De, Torrejón, C.C. De, and Ardoz, T.  
635 De (2016) Iron-rich melts, magmatic magnetite, and superheated hydrothermal systems:  
636 The El Laco deposit, Chile. *Geology*, 44, 427–430.
- 637 Tsujimori, T., Liou, J. G., Wooden, J., and Miyamoto, T. (2005) U-Pb dating of large zircons in  
638 low-temperature jadeitite from the Osayama serpentinite mélange, southwest Japan:

- 
- 639 insights into the timing of serpentinization. *International Geology Review*, 47(10), 1048-  
640 1057.
- 641 Von Gruenewaldt, G. (1994) Ilmenite-apatite enrichment in the upper zone of the Bushveld  
642 Complex: a major titanium-rock phosphate resource. *International Geology Reviews*, 35,  
643 987–1000.
- 644 Wang, M., Nebel, O., and Wang, C. Y. (2016) The Flaw in the Crustal ‘Zircon Archive’: Mixed  
645 Hf Isotope Signatures Record Progressive Contamination of Late-stage Liquid in Mafic–  
646 Ultramafic Layered Intrusions. *Journal of Petrology*, 57(1), 27–52.
- 647 Watson, E. B., and Green, T. H. (1981) Apatite/liquid partition coefficients for the rare earth  
648 elements and strontium. *Earth and Planetary Science Letters*, 56, 405–421.
- 649 Whitney, D.L., and Evans, B.W. (2010) Abbreviations for names of rock-forming minerals.  
650 *American Mineralogist*, 95, 185–187.
- 651 Widanagamage, I.H. (2011) EMPA Dating of Monazite from High Grade Metamorphic Rocks  
652 Along the Highland-Vijayan Boundary Zone, Sri Lanka. Kent State Univeristy.
- 653 Wiedenbeck, M.A.P.C., Alle, P., Corfu, F., Griffin, W.L., Meier, M., Oberli, F., Quadt, A.V.,  
654 Roddick, J.C., and Spiegel, W. (1995). Three natural zircon standards for U–Th–Pb, Lu–  
655 Hf, trace element and REE analyses. *Geostandards Newsletter*, 19, 1–23.
- 656 Woodhead, J.D., and Hergt, J.M. (2005) A preliminary appraisal of seven natural zircon  
657 reference materials for in situ Hf isotope determination. *Geostandards and Geoanalytical  
658 Research*, 29, 183–195.
- 659 Zheng, J., Griffin, W.L., O’Reilly, S.Y., Zhang, M., and Pearson, N. (2006) Zircons in mantle  
660 xenoliths record the Triassic Yangtze-North China continental collision. *Earth and  
661 Planetary Science Letters*, 247, 130–142.
- 662

663 **Figure captions:**

664 **Fig. 1** Generalized geological and tectonic framework of Sri Lanka showing the major crustal  
665 blocks, their boundaries, serpentinite localities and the sample localities. (After Cooray,  
666 1994; Rajapaksha et al. 2012; He et al. 2016).

667 **Fig. 2** (a) Detailed geological map of the study area showing the northern part of the  
668 boundary between Highland and Vijayan Complexes, together with sample localities.  
669 (Modified after Corray, 1994); (b) Geological map of Seruwila copper-magnetite deposit  
670 (Modeified after Seneviratne et al. 1998 and Brooks et al. 1985).

671 **Fig. 3** Representative field photographs of the ore and host rocks from Seruwila magnetite  
672 deposit. (a) and (b) the contact zone of ultramafic host rock with magnetite; (c) apatite-  
673 bearing disseminated magnetite ore sample; (d) massive crystalline magnetite ore  
674 sample with abundant clinopyroxene;

675 **Fig. 4** Photomicrographs showing textures of representative samples from Seruwila  
676 magnetite deposit. (a) euhedral amphibole, clinopyroxene from ultramafic host rock  
677 (VC18-4); (b) zircon grains occur as inclusions in the silicate minerals. (c) massive  
678 magnetite ore sample with assemblage of coarse-grained apatite, clinopyroxene and  
679 magnetite (sample VC18-3); (d) back scattered electron(BSE) image of spinel exsolution  
680 occurring within and along the magnetite grain boundary (VC18-3); (e) secondary  
681 actinolite growth surrounding clinopyroxene and apatite (VC18-6); (f) back scattered  
682 electron(BSE) image of spinel exsolution occurring along anhedral magnetite grain  
683 boundary (sample VC18-6); (g) clinopyroxene, magnetite, amphibole, scapolite, and  
684 apatite assemblage from Seruwila deposit transitional boundary (sample VC18-5),  
685 euhedral scapolite replaces and cuts the magnetite; (h) scapolite replace magnetite and  
686 clinopyroxene, green colored spinel exsolution from magnetite (sample VC16-3);

687 **Fig. 5** Compositional diagrams showing chemistry of representative minerals. (a) Si (pfu)

688 versus  $X_{Mg}$  diagram showing compositions of calcic amphibole (after Leake et al. 1997);  
689 (b) wollastonite-enstatite-ferrosilite diagram showing compositions of clinopyroxene  
690 and orthopyroxene (after Morimoto, 1988); (c) plots of the halogen content in apatite (in  
691 molar proportions); (d) plots of Ti vs. Ni/Cr diagram for magnetite (after Dare et al.  
692 2015).

693 **Fig. 6** Chondrite-normalized REE distribution diagram (a) and primitive-mantle-normalized  
694 multi-element variation diagram (b) for studied samples from Seruwila deposit.  
695 Normalizing values for (a) and (b) are from McDonough and Sun (1995) and Sun and  
696 McDonough (1989), respectively.

697 **Fig. 7** Cathodoluminescence (CL) images for representative zircons from the Seruwila  
698 deposit. Spot numbers,  $^{207}Pb/^{235}U$  ages (with 2 sigma error), and  $\epsilon Hf$  values where  
699 available, are also shown. The small circle represents location of LA-ICP-MS U-Pb  
700 analyses and the larger circles represent Hf isotopic analyses. All the scale bars represent  
701 100  $\mu m$ .

702 **Fig. 8** Tera-Wasserburg U-Pb concordia plots and weighted average plots for ore rock sample  
703 VC16-3 (a) and (b), for ultramafic host rock sample VC18-4 (c) and (d). Ellipses with  
704 light grey color are excluded from weighted mean age calculation. All data point  
705 uncertainties are  $2\sigma$ . The two different uncertainty values shown represent  
706 uncertainties with and without the systematic error propagated respectively.

707 **Fig. 9** Zircon Hf isotopic evolution diagram from Seruwila deposit ore and host rocks.  
708 CHUR-chondritic uniform reservoir. The corresponding lines of crustal extraction are  
709 calculated by using the  $^{176}Lu/^{177}Hf$  ratio of 0.015 for the average continental crust  
710 (Griffin et al. 2004).

711 **Fig. 10** (a) Tectonic model of Seruwila ultramafic intrusion where the magma is formed by  
712 partial melting of metasomatized volatile-rich mantle in a post-collisional extension

713 environment. (b) Schematic model for the genesis of Seruwila magnetite–apatite  
714 deposit: 1) at depth, the iron-rich melt likely separated from the parental ultramafic  
715 magma perhaps due to contrasts in density, viscosity, or volatile content; 2) tectonic  
716 stress changes (post-collisional extension/faults) cause an efficient ascent of the  
717 magnetite suspension and accumulation as massive-type magnetite; 3) progressive  
718 cooling aided by hydrothermal fluid caused the eventual growth of disseminated  
719 magnetite; 4) calcic metasomatism (scapolitization and actinolitization) developed  
720 through interaction with the proximal calc-silicates. VC–Vijayan Complex, HC–  
721 Highland Complex

722 **Tables:**

723

724

725

**Table 1. Localities, rock types and mineral assemblage of samples in this study from Seruwila magnetite–apatite deposit.**

Sample No.	Co-ordinates	Localities	Mineral assemblage
VC16/1	N08°20'45.4", E81°17'24.5"	host ultramafic rock	amp, cpx, mag, ap, zrn
VC18/4	N08°20'39.5", E81°18'39.4"	host ultramafic rock	amp, cpx, mag, ap, zrn
VC16/4	N08°20'45.4", E81°17'24.5"	massive magnetite ores	cpx, mag, spl, amp, scp, ap, zrn
VC18/3	N08°20'39.5", E81°18'39.4"	massive magnetite ores	cpx, mag, spl, amp, scp, ap, zrn
VC16/2	N08°20'45.4", E81°17'24.5"	disseminated magnetite ores	cpx, mag, amp, scp, ap, zrn
VC18/1	N08°20'39.5", E81°18'39.4"	disseminated magnetite ores	cpx, mag, amp, scp, ap, zrn
VC18/6	N08°20'39.5", E81°18'39.4"	disseminated magnetite ores	cpx, mag, spl amp, scp, ap, zrn
VC16/3	N08°20'45.4", E81°17'24.5"	transitional zone of host rock and ore body	cpx, mag, spl, amp, scp, ap, zrn
VC16/5	N08°20'45.4", E81°17'24.5"	transitional zone of host rock and ore body	cpx, mag, amp, scp, ap, zrn
VC16/6	N08°20'45.5", E81°17'24.6"	transitional zone of host rock and ore body	cpx, mag, amp, scp, ap, zrn
VC18/2	N08°20'39.5", E81°18'39.4"	transitional zone of host rock and ore body	cpx, mag, amp, scp, ap, zrn
VC18/5	N08°20'39.5", E81°18'39.4"	transitional zone of host rock and ore body	cpx, mag, amp, scp, ap, zrn

726 Mineral abbreviations follow Whitney & Evans, 201

727

**Table 2 LA-ICP-MS zircon Lu–Hf isotope data of for samples in this study.**

Sample spots	Age (Ma)	<sup>176</sup> Yb/ <sup>177</sup> Hf	<sup>176</sup> Lu/ <sup>177</sup> Hf	<sup>176</sup> Hf/ <sup>177</sup> Hf	2s	<sup>176</sup> Hf/ <sup>177</sup> Hf <sub>i</sub>	ε <sub>Hf</sub> (0) *	ε <sub>Hf</sub> (t) †	T <sub>DM</sub> (Ma) ‡	2s T <sub>DM</sub> (Ma) §	f <sub>Lu/Hf</sub> ¶
VC16-3-01	541.5	0.00386	0.000135	0.282382	0.000018	0.282381	-13.8	-1.9	1203	1623	-1.00
VC16-3-05	521.0	0.003341	0.000124	0.282368	0.000018	0.282367	-14.3	-2.9	1222	1667	-1.00
VC16-3-06	524.7	0.004586	0.000168	0.282356	0.000018	0.282354	-14.7	-3.2	1239	1692	-0.99
VC16-3-07	516.9	0.004907	0.000179	0.282392	0.000022	0.282390	-13.4	-2.1	1190	1617	-0.99
VC16-3-08	532.3	0.004478	0.000166	0.282339	0.000018	0.282337	-15.3	-3.7	1263	1726	-1.00
VC16-3-09	536.0	0.004616	0.000175	0.282398	0.000020	0.282396	-13.2	-1.5	1182	1591	-0.99
VC18-4-03	517.1	0.002037	0.00008	0.282406	0.000022	0.282405225	-12.9	-1.6	1168	1583	-1.00
VC18-4-04	539.9	0.002387	0.000098	0.282482	0.000016	0.282481	-10.3	1.6	1064	1399	-1.00
VC18-4-06	584.1	0.015184	0.000584	0.282439	0.000014	0.282432603	-11.8	0.9	1138	1479	-0.98
VC18-4-07	531.2	0.003274	0.000135	0.282471	0.000022	0.282469656	-10.6	1.0	1081	1430	-1.00
VC18-4-18	522.8	0.007562	0.000288	0.282447	0.000022	0.282444178	-11.5	-0.1	1118	1492	-0.99

\*:  $\epsilon_{Hf}(0) = ((^{176}Hf/^{177}Hf)_S / (^{176}Hf/^{177}Hf)_{CHUR,0} - 1) \times 10,000$ ;

†  $\epsilon_{Hf}(t) = ((^{176}Hf/^{177}Hf)_S - (^{176}Lu/^{177}Hf)_S \times (e^{\lambda t} - 1)) / ((^{176}Hf/^{177}Hf)_{CHUR,0} - (^{176}Lu/^{177}Hf)_{CHUR,0} \times (e^{\lambda t} - 1)) \times 10,000$ ;

‡ Single-stage depleted mantle model age:  $T_{DM} (Ma) = 10000/\lambda \times \ln(1 + ((^{176}Hf/^{177}Hf)_S - (^{176}Hf/^{177}Hf)_{DM}) / ((^{176}Lu/^{177}Hf)_S - (^{176}Lu/^{177}Hf)_{DM}))$ ;

§ Two-stage depleted mantle model age:  $2s T_{DM} (Ma) = T_{DM1} - (T_{DM1} - t) \times ((^{176}Lu/^{177}Hf)_{CHUR} / (^{176}Lu/^{177}Hf)_{CHUR} - (^{176}Lu/^{177}Hf)_{DM} / (^{176}Lu/^{177}Hf)_{DM}) / (1/\lambda \times \ln(1 + ((^{176}Hf/^{177}Hf)_S - (^{176}Hf/^{177}Hf)_{DM}) / ((^{176}Lu/^{177}Hf)_S - (^{176}Lu/^{177}Hf)_{DM}))) + t$ ;

¶  $f_{Lu/Hf} = ((^{176}Lu/^{177}Hf)_S / (^{176}Lu/^{177}Hf)_{CHUR} - 1) / (t \times \lambda - 1.865 \times 10^{-11} \text{ year}^{-1} \text{ (Scherer et al., 2001; Söderlund et al. 2004)}) + ((^{176}Lu/^{177}Hf)_{CHUR} - (^{176}Lu/^{177}Hf)_{DM}) / ((^{176}Lu/^{177}Hf)_{CHUR} - (^{176}Lu/^{177}Hf)_{DM}) - 1$ ;  $(^{176}Lu/^{177}Hf)_{CHUR,0} = 0.015$ ,  $(^{176}Lu/^{177}Hf)_{DM} = 0.0384$ ,  $(^{176}Hf/^{177}Hf)_{DM} = 0.28325$  (Griffin et al. 2000);  $(^{176}Lu/^{177}Hf)_{CHUR} = 0.0332$ ,  $(^{176}Hf/^{177}Hf)_{CHUR,0} = 0.282772$  (Blichert-Toft and Albare' de 1997);  $(^{176}Lu/^{177}Hf)_S$  and  $(^{176}Hf/^{177}Hf)_S$  are measured values of samples).

728



Fig. 1

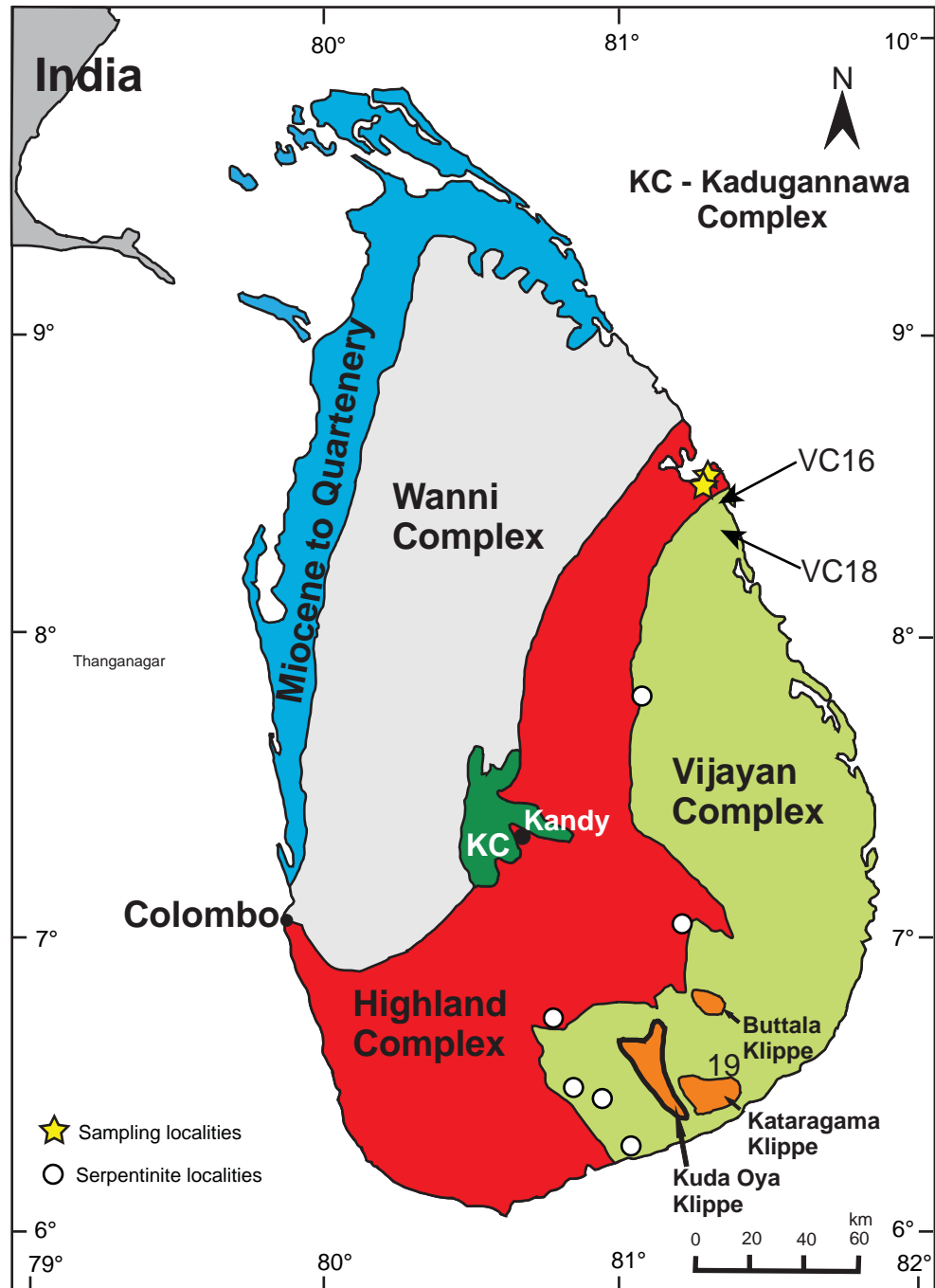


Fig. 2

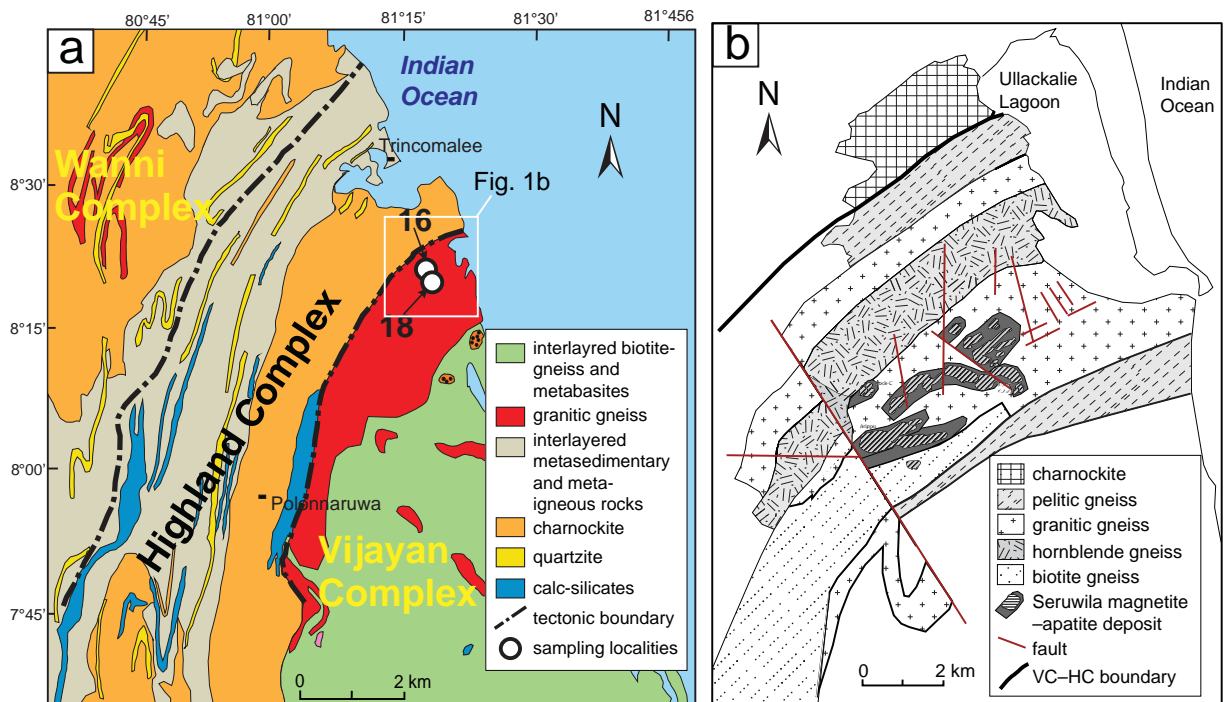


Fig. 3

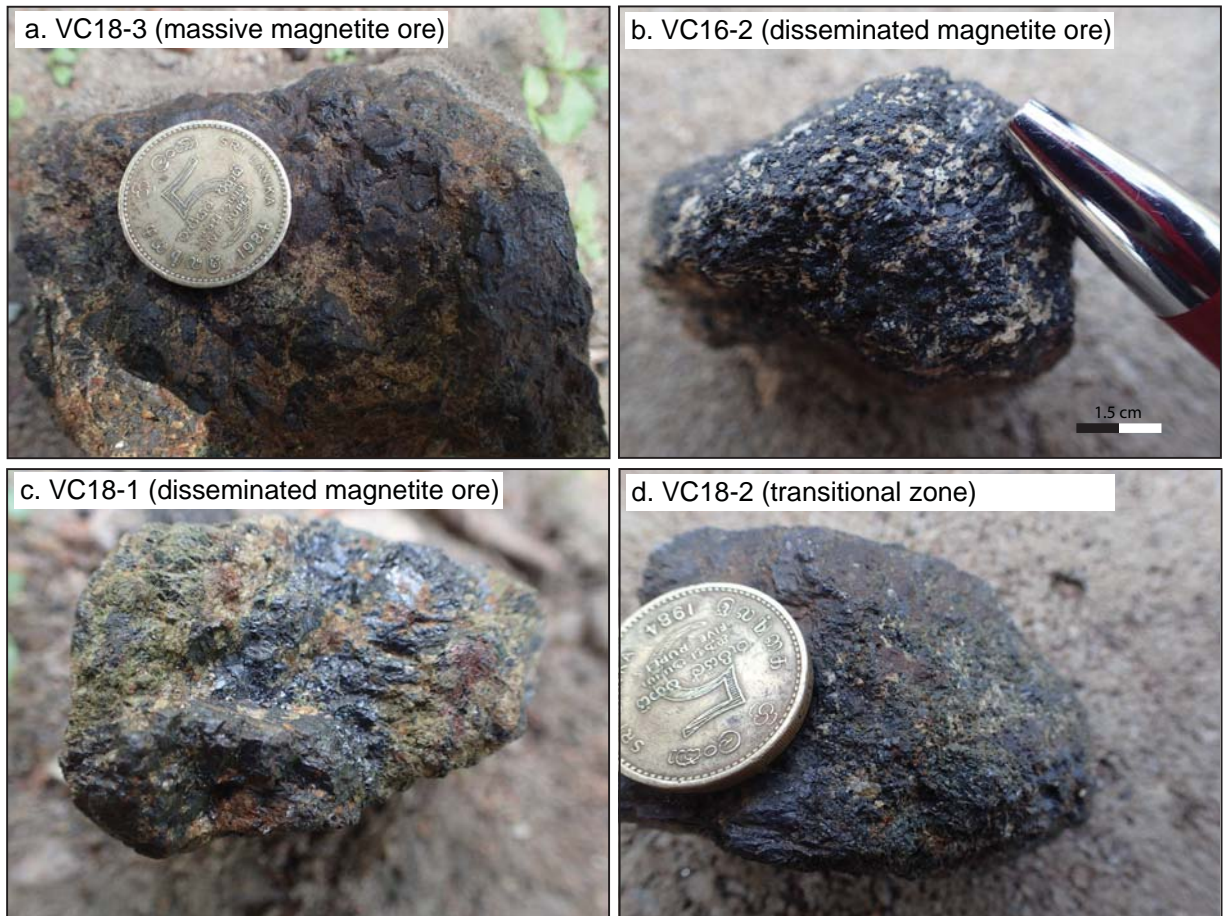
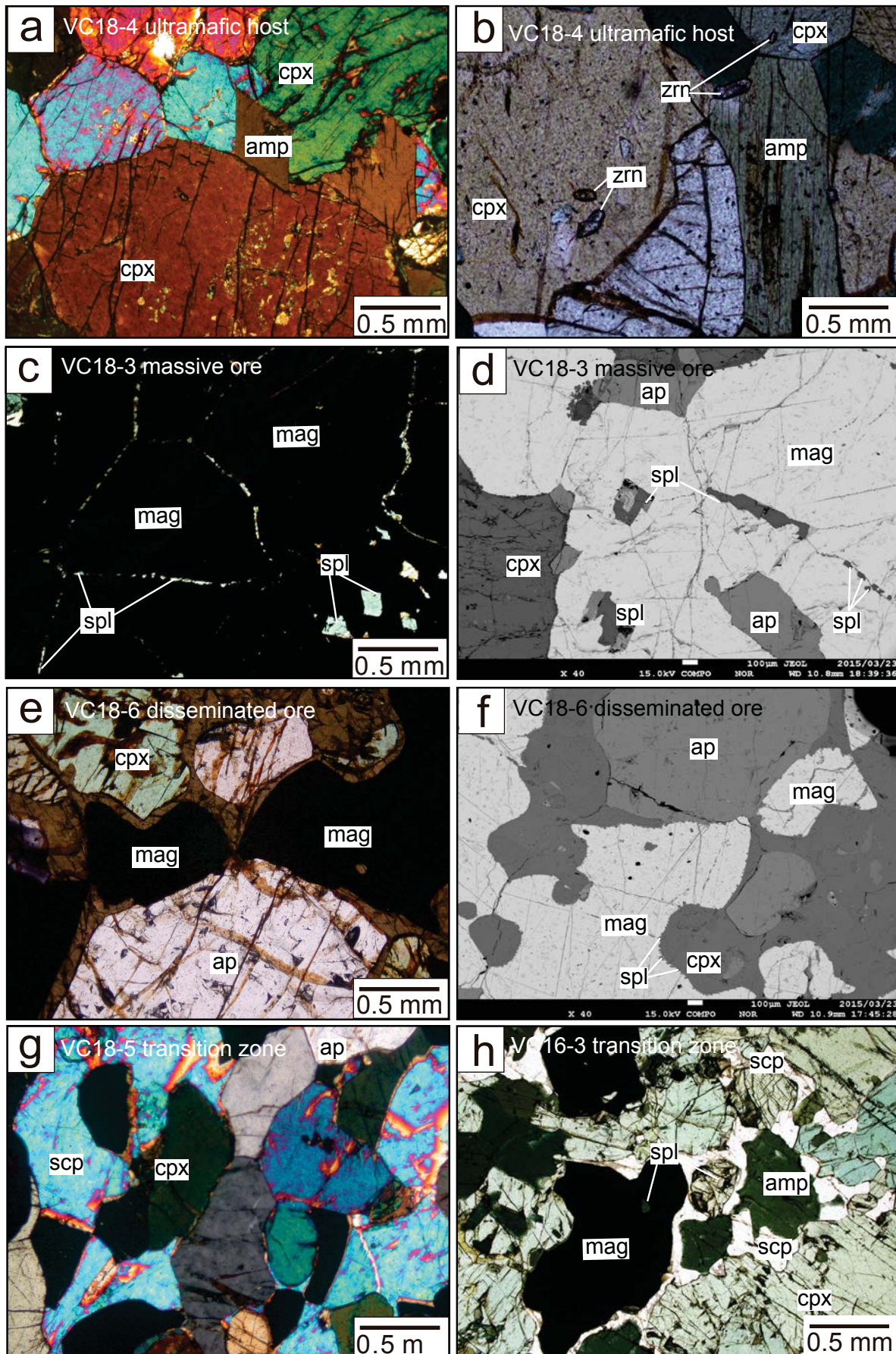




Fig. 4



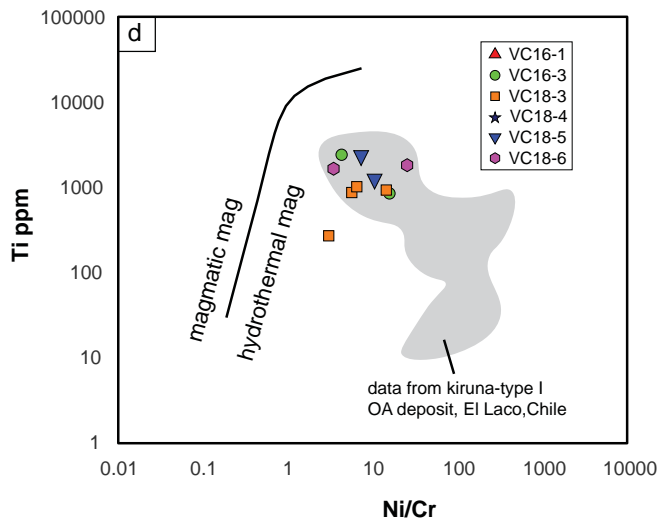
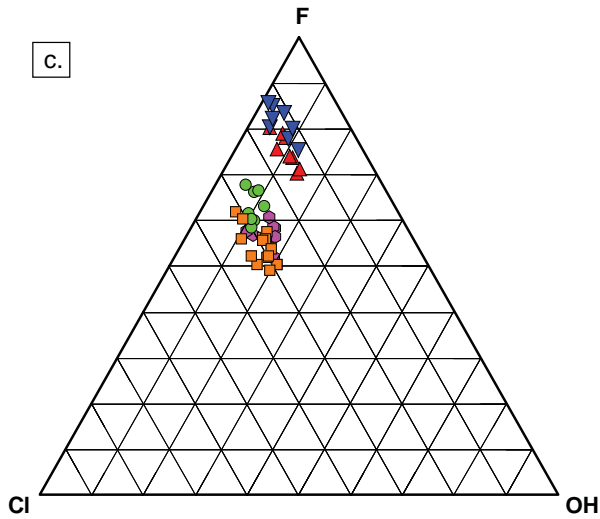
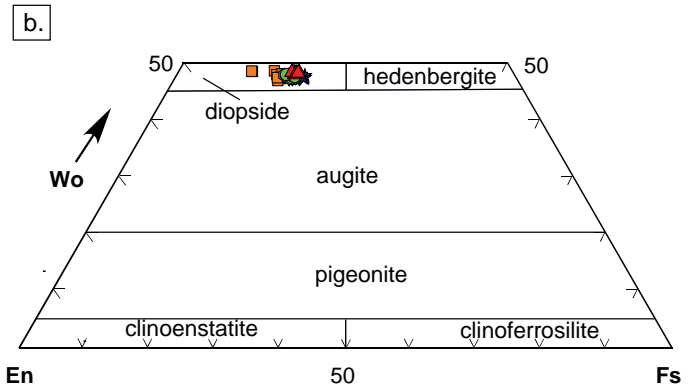
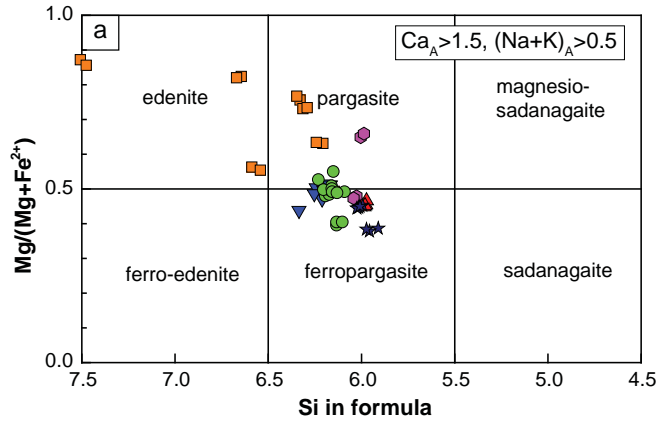


Fig. 6

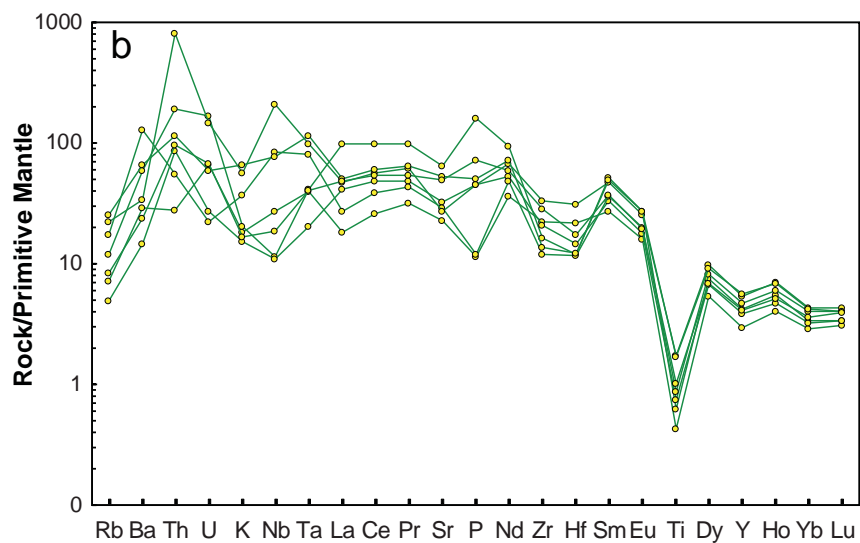
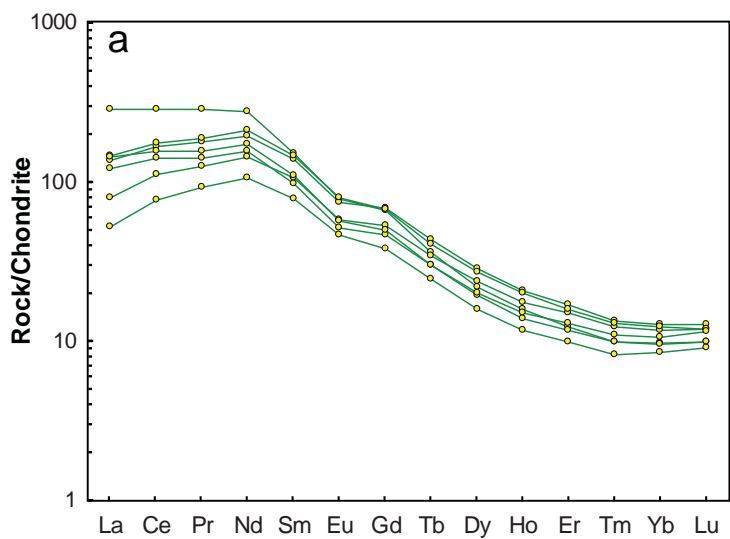


Fig. 7

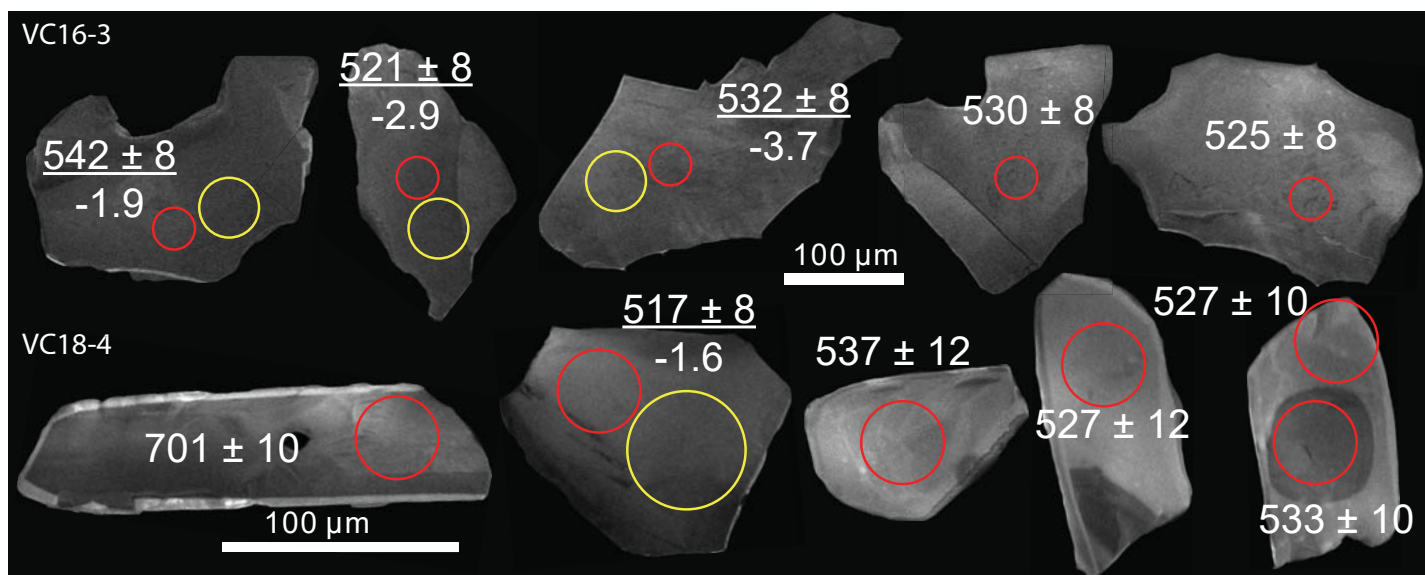




Fig. 8

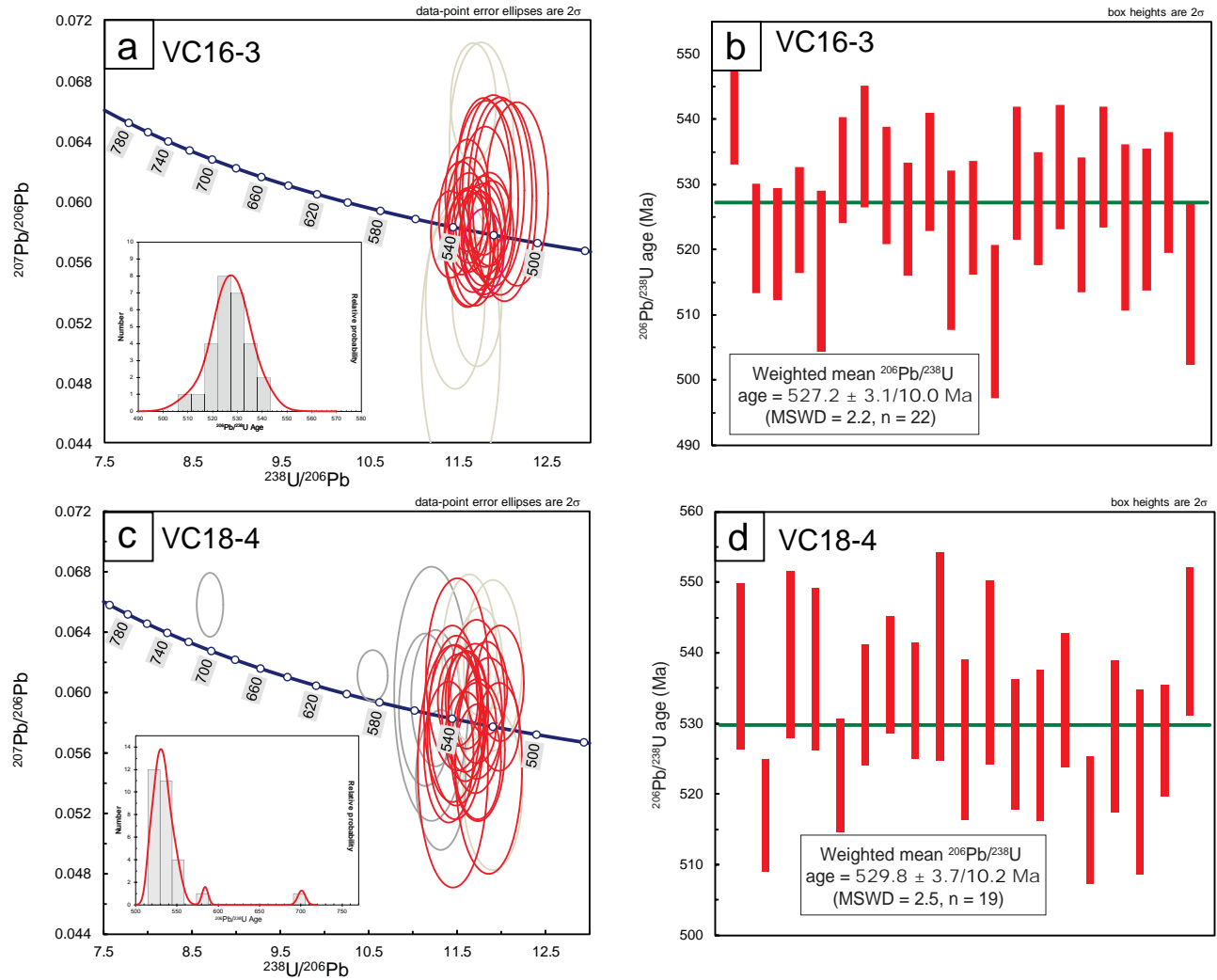




Fig. 9

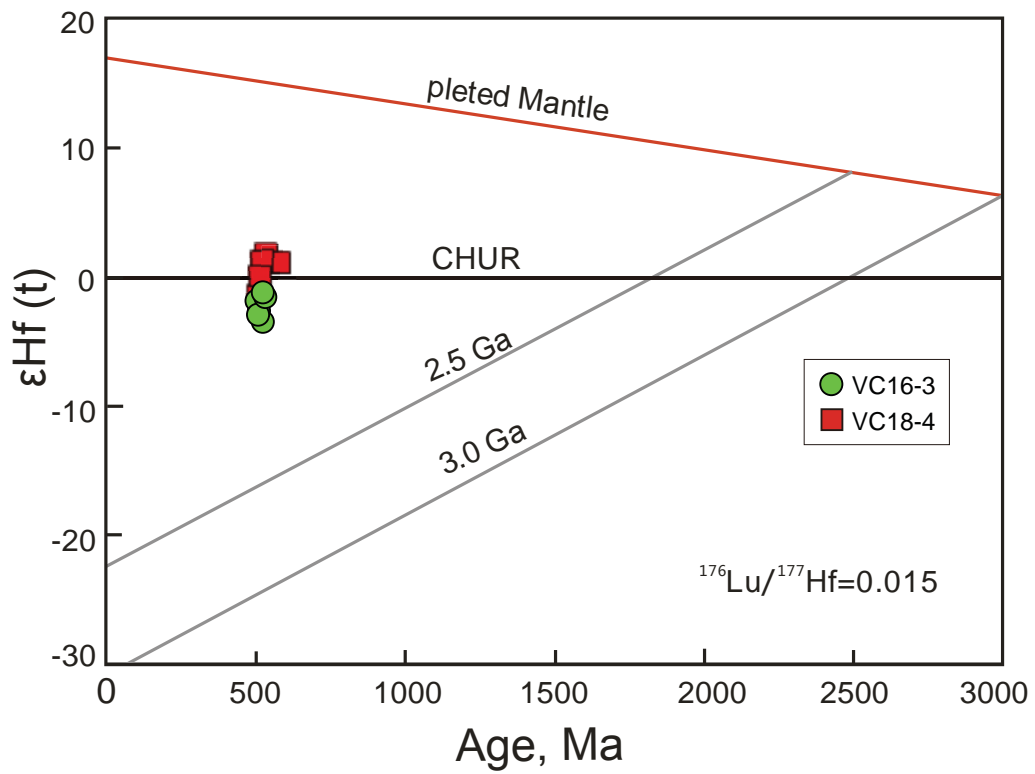


Fig. 10

